THE ASTROPHYSICAL JOURNAL, 432:103–113, 1994 September 1

INVERSE COMPTON X-RAY EMISSION FROM THE SUPERLUMINAL QUASAR 3C 345

S. C. UNWIN
Owens Valley Radio Observatory, California Institute of Technology 105-24, Pasadena, CA 91125
A. E. WEHRLE
Infrared Processing and Analysis Center, Jet Propulsion Laboratory, California Institute of Technology 100-22, Pasadena, CA 91125
C. M. URRY AND D. M. GILMORE
Space Telescope Science Institute, 3700 San Martin Drive, Baltimore, MD 21218
E. J. BARTON AND B. C. KJERULF
Owens Valley Radio Observatory, California Institute of Technology 105-24, Pasadena, CA 91125
J. A. ZENSUS
National Radio Astronomy Observatory, P.O. Box 0, Socorro, NM 87801
AND
C. R. RABAÇA
University of Alabama, Department of Physics and Astronomy, Box 870324, Tuscaloosa, AL 35487-0324
Received 1993 November 18; accepted 1994 March 3

ABSTRACT

In quasars with strong radio cores, the inverse-Compton process is believed to be the dominant source X-ray emission. For objects with parsec-scale radio jets, simple models have predicted that components in the jet emerging from the quasar nucleus generate the observed X-ray emission. We have tested this hypothesis in detail for the quasar 3C 345 using a *ROSAT* X-ray observation in 1990 July, together with quasi-simultaneous VLBI imaging of the parsec-scale jet at five frequencies. The *ROSAT* spectrum is well fitted by a power law with index $\alpha = -0.96 \pm 0.13$, consistent with models in which the X-ray emission results from inverse-Compton scattering of radio radiation from high-energy electrons in compact components.

We show that the radio properties of brightest "knot" in the jet ("C5") can be fitted with a homogeneous sphere model whose parameters require bulk relativistic motion of the emitting material; otherwise the predicted inverse-Compton X-ray emission exceeds the observed flux. If C5 is the origin of the X-ray emission, then it has a Doppler factor $\delta = 7.5^{+3}_{-2}$. If the nucleus or other components contribute to the X-ray emission, then this becomes a firm lower limit to δ. The inhomogeneous jet model of Königl is a good fit both to the barely resolved (<1 pc) flat-spectrum nucleus in the radio, and also to the *ROSAT* X-ray spectrum. The synchrotron and inverse-Compton emitting fluid moves down a narrow cone (opening angle $2\phi \approx 5°$) nucleus relativistically, with $\delta \approx 4.6$.

Doppler factors for the nucleus and C5, derived from our *ROSAT* observation, provide evidence for bulk relativistic motion in the jet. By combining these constraints with the well-known superluminal motion of jet components, we can deduce the jet geometry. For epoch 1990.5 we infer the Lorentz factor $\gamma = 7.5^{+1.0}_{-1.5}$ and angle to the line of sight $\theta = 8^{+2°}_{-3°}$ for $H_0 = 100$ km s^{-1} Mpc^{-1}. These values are the most reliable yet derived using this method, because of the near-simultaneity of our X-ray and VLBI observations and the quality of the multifrequency VLBI images and component radio spectra.

Subject headings: galaxies: jets — quasars: individual: (3C 345) — radiation mechanisms: nonthermal — radio continuum: galaxies — X-rays: galaxies

1. INTRODUCTION

The quasar 3C 345 ($z = 0.595$) has been imaged with VLBI at several radio frequencies since 1977, and the detailed evolution of its parsec-scale relativistic jet has been well characterized (Unwin et al. 1983; Biretta, Moore, & Cohen et al. 1986, hereafter BMC; Zensus, Cohen, & Unwin 1994, hereafter ZCU). It is probably the best-studied "core-jet" source (with its "superluminal" nature first noted by Moffet et al. 1972), though a number of surprising features have recently been revealed in new high dynamic range images (Unwin & Wehrle 1992, hereafter UW92). 3C 345 shows variability over a wide range of frequencies and it classified as a blazar by Impey & Neugbauer (1988) and as a high-polarization quasar by Moore & Stockman (1981). Published X-ray data show it to be weak in X-rays and provide some evidence of variability, though comparison is difficult because the detections were in different energy bands: by the *Einstein Observatory* (Ku, Helfand, & Lucy 1980) and by *Ginga* (Makino 1989). A search of the High Energy Astrophysics Science Archive Research Center BROWSE database showed that no observation was made by *EXOSAT*. The archival X-ray data are summarized in Table 1.

The radio spectrum and polarization of blazars like 3C 345 suggest that synchrotron radiation dominates the radio emission. Radio imaging typically reveals one or more high-brightness temperature components, in the form of unresolved sources or a tightly collimated one-sided jet (Pearson 1990). The rapid variability of blazars at many wavelengths also implies that the nonthermal emission over a wide frequency range must be emitted in a very small volume, most likely close to the central energy source, which is presumed to be a massive

TABLE 1

X-RAY OBSERVATIONS OF 3C 345

Epoch	Instrument	Observed Band (keV)	Flux Density at 1 keV[a] (μJy)	Spectral Index	$N_{H\,I}$[b] (10^{20} cm^{-2})	Reduced χ^2	References
1979.96	*Einstein* IPC	0.1–3.5	$0.7^{+0.12}_{-0.08}$	$-0.43^{+0.24}_{-0.46}$	0.74	1.38	1
1980.12	*Einstein* MPC	2–10	0.90 ± 0.45	-0.35 ± 0.30	...	...	2
1989.32	*Ginga* LAC	2–10	0.57	-0.40 ± 0.09	...	...	3
1990.55	*ROSAT* PSPC	0.2–2.0	0.39 ± 0.03	-0.89 ± 0.07	0.74	1.20	4
1990.55[c]	*ROSAT* PSPC	0.2–2.0	0.39 ± 0.03	$-0.85^{+0.22}_{-0.24}$	$0.67^{+0.55}_{-0.46}$	1.24	4

[a] All errors in this table represents 90% confidence ranges. MPC and LAC fluxes interpolated from 2 keV, with estimated errors which include contributions from uncertainty in spectral index.

[b] Absorbing H I column density used in spectral fit; values for MPC and LAC not specified. For IPC and PSPC, $N_{H\,I}$ was fixed at the Galactic value measured by Elvis, Lockman, & Wilkes 1989.

[c] Spectral fit parameters for PSPC, but treated $N_{H\,I}$ as a free parameter.

REFERENCES.—(1) Worrall & Wilkes 1990; (2) Halpern 1982; (3) Makino 1989; (4) this paper.

black hole (Blandford & Rees 1992). Together the high-brightness temperatures and rapid variability imply that inverse-Compton scattering of radio (or optical) photons into the X-ray range will be important (e.g., the synchrotron self-Compton, or SSC, model; Jones, O'Dell, & Stein 1974; Blandford & Königl 1979; Celotti, Maraschi, & Treves 1991), particularly in radio-bright blazars like 3C 345. Ghisellini et al. (1993) applied these principles in a comprehensive statistical study of over 100 sources for which VLBI measurements of the radio cores are available and found broad support for the "standard" relativistic twin-jet model. In a few cases (typically the less radio-bright blazars), the X-ray emission may be dominated by direct synchrotron radiation, depending on the electron energies and the magnetic field strength. Distinguishing between these two mechanisms should be possible with spectral information at X-ray and radio or optical wavelengths.

We undertook a program of observations using the Position-Sensitive Proportional Counter (PSPC) on *ROSAT* (Pfeffermann et al. 1986) to derive a high signal-to-noise ratio soft X-ray spectrum of 3C 345, to test SSC models. Because the physical parameters of compact radio components are a key feature of such models (Cohen 1985; Marscher 1980; Königl 1981; Ghisellini, Maraschi, & Treves 1985), we have made VLBI images which are almost contemporaneous with the *ROSAT* observation. 3C 345 has a long history of high-quality VLBI observations (Unwin et al. 1983; UW92), which makes it one of the best targets for a detailed examination of X-ray model predictions. Detailed SSC-jet models have been proposed to explain broad trends in the electromagnetic spectrum (e.g., Maraschi, Ghisellini, & Celotti 1992; Hutter & Mufson 1986; Band & Grindlay 1986; Marscher & Gear 1985), but because these models all introduce additional degrees of freedom, they can be tested only with additional data. Multi-waveband monitoring (e.g., Webb et al. 1994) constrains many of these parameters; the Webb et al. data are not directly applicable to the present work as they refer to approximately mid-1991.

Meaningful comparisons between jet models and VLBI images are often problematic. Except for sources with very simple parsec-scale structure, comparisons with SSC models may be dominated by unknown systematic errors due to incomplete data. Quasi-simultaneous multiwavelength VLBI observations, like those we present here for 3C 345, are essential for reliable spectral and spatial decomposition of the radio emission. Several tens of VLBI images of 3C 345 have been made over the years (Unwin et al. 1983; BMC; ZCU)—more than for any other VLBI target—and we use this database to check that the spectra we derive are plausible. The core-jet structure of 3C 345 is by no means unusual among compact flat-spectrum radio sources (see, e.g., Peason & Readhead et al. 1988), so this note of caution applies to modeling of any core-dominated quasar.

In this paper we adopt a "combined" model to represent the structures seen with VLBI: (1) "knots" in the jet are modeled as homogeneous spheres (Cohen 1985), and (2) the unresolved "core" is represented as a conical two-sided jet with power-law dependences of the particle density and magnetic field with radius (Königl 1981). The Königl model was first developed to explain the relatively flat radio spherical index found in the cores of radio-loud quasars; this certainly applies to 3C 345, and the model fits our observations very well, as we show below. The knots are thought to be shocks or other disturbances in the jet flow. A sphere is a poor approximation to a shock, but there is insufficient resolution, even with high-frequency VLBI, to map out shocks in any detail, but differences in emission between spherical and slab geometry is only of order a factor of 2 (Band & Grindlay 1985; Hughes & Miller 1991). Doppler boosting may also change the appearance of a shock relative to the underlying flow. In any case, the spherical model provides a useful probe of the jet kinematics (see § 4.1 below).

This combined model (as used by ZCU) has a number of virtues, besides relative simplicity. First, it provides a means of explicitly including VLBI morphology in the model, by adding spheres as necessary to represent the principal compact components in the jet (those most likely to generate X-rays). Second, it makes a specific prediction of the X-ray flux density and spectrum which can be verified. Third, since other mechanisms may contribute to the X-ray emission, the inverse-Compton flux predicted by each component can be compared separately to the measured X-ray flux. Fourth, long-term variability in X-rays provides a powerful additional test of the SSC model since predictions based on the changing VLBI morphology must agree with any observed X-ray variations. Results of our project to monitor 3C 345 for X-ray variability with subsequent *ROSAT* observations will be reported elsewhere.

Our *ROSAT* observations are presented in § 2, and § 3 describes the VLBI imaging observations. In § 4 we apply simple SSC models to the X-ray and ratio data, discuss how

well they match observation, and derive the jet kinematics and orientation. We also compute the equipartition Doppler factor and deduce the physical conditions in the components. We summarize our results and discuss the implications in § 5. Throughout this paper, we use a Hubble constant $H_0 = 100\ h$ km s^{-1} Mpc^{-1} and $q_0 = 0.5$; for $z = 0.595$, the angular scale is 3.79 h^{-1} pc mas^{-1}, and the luminosity distance is $D_l = 1.99$ Gpc. Where necessary, we set $h = 1$ and convert published quantities to this value. The radio definition of spectra index α ($S \propto \nu^{\alpha}$) is also used in the X-ray band; the X-ray photon index is $\Gamma = 1 - \alpha$.

2. *ROSAT* OBSERVATIONS

We observed 3C 345 with the *ROSAT* PSPC-C instrument in one of its very first pointed observations, during the Pre-measurement, Calibration, and Verification phase, before the all-sky survey commenced. The exposure of 4086 s was made in two almost equal periods on 1990 July 19 and 20. The quasar was positioned close to the center of the detector field so vignetting is negligible; a number of other objects, some of which are identified with stars, are present in the field, but none are close enough to cause any difficulty in extracting the source and background photon counts from the image. The background was selected as an annular region around the quasar with inner radius 1.'1 and outer radius 15.'2 (i.e., within the central "ring") but excluding several visible sources in the field. Source extraction and background subtraction were done using the PROS/IRAF package (Worrall et al. 1992) which applies instrumental corrections such as time-dependent pointing offsets. Data from the two exposures (of 1780 s and 2306 s, respectively) were extracted and analyzed separately; the fitted flux densities differed by only 1% so the two intervals were combined for further analysis. Only the summed spectrum, shown in Figure 1, is discussed in the rest of this paper.

The source was unresolved, to within the telescope and detector resolution, and spacecraft pointing. The point-spread function is about 25″ FWHM (Hasinger et al. 1992); our limit to the angular size is $\lesssim$20″, which is much larger than the known 4″ radio jet (Kollgaard, Wardle, & Roberts 1989), and comparable to the diffuse 20″ radio halo (Murphy, Browne, & Perley 1993). A reliable detection of variability would eliminate the possibility that the X-ray emission originates in the arcsecond-scale jet or halo. We have some evidence for variability between the *Einstein* and *ROSAT* observations (see below); in this paper we assume that the emission originates in the vicinity of the high-brightness radio components images with VLBI (i.e., $\ll$0.''1). A number of blazars are variable in X-rays on short timescales, which argues in favor of this interpretation, since inferred sizes are no larger than the measured VLBI size scales.

To fit the PSPC spectrum of 3C 345 we used the XSPEC spectral fitting software (Shafer et al. 1990). A number of different models were tried, including thermal blackbody, bremsstrahlung, and a power law, all including an absorbing H I column. Only power-law models yielded reasonable fits. Spectral fitting results are summarized in Table 1. 3C 345 has a very low Galactic H I column density along its line of sight to Earth ($N_{\rm H\,I} = 0.74 \times 10^{20}$ cm^{-2}; Elvis, Lockman, & Wilkes 1989). Because the PSPC is insensitive to energies $\lesssim$0.2 keV, and because absorption in our spectrum is weak, the absorbing column density is not determined very accurately. Figure 1 shows the best-fitting power-law model (convolved with the PSPC-C response matrix of 1993 January 12), and Figure 2 shows a likelihood plot of H I column density versus photon index. Best-fit model values for $N_{\rm H\,I}$, α, and normalization (observed spectral flux density at 1 keV) are given in Table 1.

Note that the fitted $N_{\rm H\,I}$ is very close to the Galactic value; fixing it at that value yields $\alpha = -0.89 \pm 0.07$, and an integrated incident flux before any absorbing column of $(2.06 \pm 0.16) \times 10^{-12}$ ergs cm^{-2} s^{-1} in the 0.2–2.0 keV observed band (90% confidence ranges). We also solved for an absorbing H I column at the redshift of the source, but it was poorly constrained, with an approximate upper limit of $N_{\rm H\,I} \lesssim 2.2 \times 10^{20}$ cm^{-2} for any absorption intrinsic to the source.

The fit parameters are somewhat sensitive to the energy range included. Parameters listed in Table 1 were derived using range shown in Figure 1; the fit is poor below about 0.25 keV.

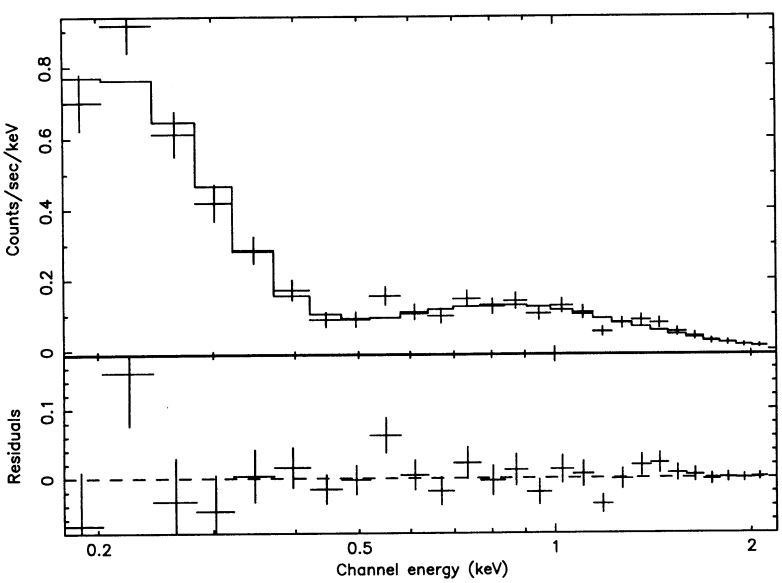

FIG. 1.—X-ray spectrum of 3C 345 taken with the *ROSAT* PSPC, 1990 July 19–20. Error bars were derived from photon statistics. Also shown is the fit (*solid curve*) of the best-fit free-$N_{\rm H\,I}$ power-law model discussed in the text, with $\alpha = -0.85$ and $N_{\rm H\,I} = 0.67 \times 10^{20}$ cm^{-2}. Lower panel shows the residuals to this fit.

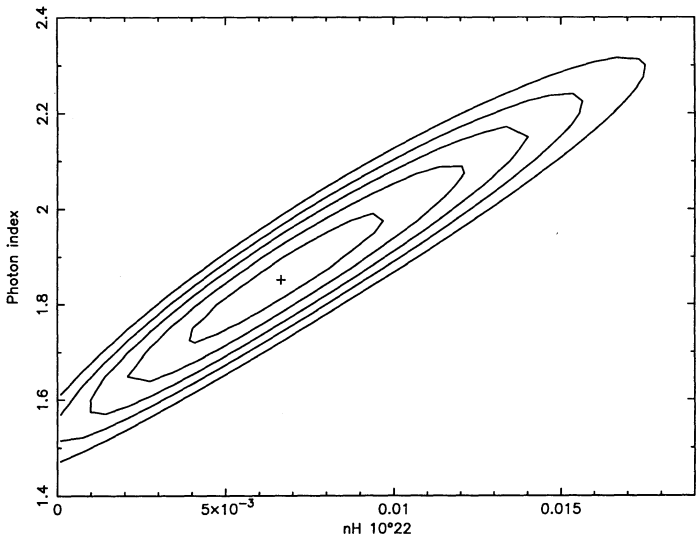

FIG. 2.—Confidence contours for the spectral fit, as a function of neutral hydrogen absorbing column $N_{\rm H\,I}$ and photon index ($\Gamma = 1 - \alpha$). Contours are drawn at $\Delta\chi^2 = 1.00$, 2.71, 4.61, 6.63, and 9.21. These correspond respectively to 68% confidence for one parameter of interest, 90% for one, 90% for two, 99% for one, and 99% for two parameters. The best-fit value of $N_{\rm H\,I}$ is very close to the measured Galactic value of 0.74×10^{20} cm^{-2}; fixing the column at this value yields a slightly softer best-fit spectral index of $\Gamma = 1.89$.

Including data down to 0.13 keV results in a higher Galactic column $N_{\rm H\,I} = (1.53^{+0.58}_{-0.48}) \times 10^{20}$ cm^{-2} and softer spectral index of $\alpha = -1.16^{+0.21}_{-0.23}$ (90% confidence ranges), but the differences are of low statistical significance. We tried fitting the spectrum with a "broken" power-law model, with the break frequency and second photon index as additional free parameters; this did not improve the fit, so there is no evidence in our data for spectral curvature.

Table 1 includes a comparison of the *ROSAT* results with published detections of 3C 345 in the harder X-ray bands of *Einstein* (IPC and MPC) and *Ginga*. Direct comparison of fluxes is difficult because different spectral indices were fitted; we took 1.0 keV as the reference energy for convenience, though this requires minor extrapolation from the harder bands. Note that the Worrall & Wilkes (1990) flux reflects a revised *Einstein* IPC calibration compared to the original work of Ku et al. (1980).

Comparison of the IPC and PSPC fluxes, for which the observed energy bands are similar, shows that the soft X-ray flux of 3C 345 declined by nearly a factor of 2 in the 10 years between the *Einstein* and *ROSAT* observations. Comparison of the *Einstein* MPC and *Ginga* LAC which again have overlapping energy ranges, suggests a 30% decline over about 9 years. Besides getting fainter, the X-ray spectrum of 3C 345 appears to have softened substantially, from $\alpha = -0.4$ in 1979 through 1989, to $\alpha = -0.9$ in 1990. This agrees with the trend found in blazars that their spectra are slightly harder when brighter (George, Warwick, & Bromage 1988; Sembay et al. 1993; Giommi et al. 1991). During the same time period, the 15 GHz (total) radio flux density first increased, then declined, with a total variation of more than a factor of 3 (H. D. Aller & M. F. Aller, private communication). As noted above, our data show no evidence of variability on a timescale of a day, at the few percent level. In the context of SSC X-ray models, it is surprising that larger variations on timescales of a few years are not seen, especially considering the large variations in the compact radio components during this period (see light curves for components C4, C5, and D, in ZCU).

3. VLBI OBSERVATIONS

We observed 3C 345 using the US and European VLBI Networks in 1990 and 1991 as part of a continuing program of monitoring its changing parsec-scale structure in the radio. We present here only those observations closest to 1990 July, the epoch of the *ROSAT* pointing. The purpose of our analysis is to derive quasi-simultaneous multifrequency spectra and angular sizes for the compact VLBI components. Very few comparisons of expected versus measured inverse-Compton emission have used quasi-simultaneous X-ray and VLBI data (e.g., for the quasar NRAO 140, Marscher & Broderick 1985; and for 3C 279, Wehrle et al. 1994).

Details of the observing sessions, frequencies, polarization, and total flux density are given in Table 2. The telescope arrays are listed in Table 3. We used the NRAO[1] Mark II recording system, whose 2 MHz bandwidth provides adequate sensitivity for this strong radio source. Data were correlated using the JPL/Caltech Block II Correlator, and averaged in time and frequency using NRAO AIPS software. Editing, calibration, and mapping were done using the Caltech VLBI Package (Pearson 1991); see UW92 for details of the analysis procedures used. No evidence was found for "nonclosing" amplitude errors.

Figures 3–7 show CLEAN images from each of the five VLBI observations, contoured in approximately logarithmic intervals of surface brightness. As is well known from a number of VLBI imaging observations (e.g., Reid et al. 1989), map reliability is not constant but varies across the image, with spurious features tending to appear ≈ 1 beamwidth away from strong features. Figure captions indicate the reliability of each image, in terms of the brightest feature judged to be spurious. In each case, the lowest contour is somewhat higher than the theoretical (thermal) noise level, indicating that the images are ultimately limited by systematic errors rather than antenna

[1] The National Radio Astronomy Observatory is operated by Associated Universities, Inc., under cooperative agreement with the National Science Foundation.

TABLE 2

VLBI OBSERVING SESSIONS

Session	Epoch	Number of Antennas[a]	Frequency (MHz)[b]	Polarization (IEEE)	Total Flux Density (Jy)[c]
1	1990.16	7	10649.99	LCP	5.2 ± 0.1
2[d]	1990.18	15	4990.99	LCP	6.6 ± 0.2
3	1990.41	10	22228.99	LCP	5.1 ± 0.1
4	1990.73	12	1662.99	LCP	7.9 ± 0.2
5	1990.84	9	8416.99	RCP	5.1 ± 0.2

[a] Only includes those antennas yielding usable data.
[b] DC edge of recorded band; all sessions used 2.0 MHz upper sideband.
[c] Measured by Effelsberg and Owens Valley during VLBI observations.
[d] Observation from UW92.

sensitivity, a situation typical of VLBI images of strong sources. The 1.7 GHz image in particular is less reliable than the others, because only 25 minutes of data (a calibration "snapshot") were obtained, as part of a project unrelated to our long-term monitoring program. It is included here because it is almost contemporaneous, and because of its importance in constraining the low-frequency spectra of components identified on the other images.

3.1. *Analysis of the VLBI Images*

Features of the VLBI images presented in Figures 3–7 can be identified by comparison with the existing database of images of 3C 345 (BMC; UW92; ZCU). It is not clear whether regions of enhanced brightness on the images represent physical regions of emitting plasma, shocks in an underlying smooth (and weakly radiating) relativistic flow, or the results of entrainment of material from the confining medium surrounding the jet. Nevertheless, identifiable features persist from epoch to epoch; furthermore, these features (variously termed "components," "knots," or "blobs") are recognizable across a wide frequency range. We therefore label the components on the images as "D," "C6," "C5," etc., following the convention of previous papers (e.g., Unwin et al. 1983), and extrapolating measured proper motions as necessary. Component "D" is the unresolved eastern end of the source, which we identify with the nucleus, and jet features are labeled "Cn" with "n" decreasing with distance from the nucleus (or increasing with time, at a fixed radius).

3.2. *Model Fitting*

In addition to the images discussed above, we made multicomponent model fits to the data. The iterative MODELFIT procedure (Pearson 1991) performs a least-squares fit to the VLBI data in the (u, v) plane (rather than the image plane) by varying a selected subset of the model parameters. Starting parameters for each model were carefully chosen using the "final" image (made after self-calibration), as discussed by BMC. Components were taken to be homogeneous optically thin spheres, except at 1.7 GHz, where the core was assumed to be optically thick. Such models have some important advantages over images, especially for the analysis of the X-ray emission discussed below: (1) they represent the sky as much simpler than CLEAN images; (2) model components are necessarily positive, unlike CLEAN components; (3) models can represent extended emission better and are zero outside the regions of interest; and (4) this allows a more convenient derivation of component parameters. In particular, simple SSC X-ray models (e.g., Cohen 1985) which have been widely used

TABLE 3

VLBI ANTENNAS

Observatory	Location	ID	Antenna Diameter (m)	Sessions[a]
Onsala Space Observatory	Onsala, Sweden	T	20	3, 5
Onsala Space Observatory	Onsala, Sweden	S	26	2
Max-Planck-Institut für Radioastronomie	Effelsberg, Germany	B	100	2, 3, 4, 5
Westerbork Synthesis Radio Telescope	Netherlands	W	25 (14 antennas)	2, 4
Nuffield Radio Astronomy Laboratory	Jodrell Bank, UK	J	76	4
Istituto di Radioastronomia	Medicina, Italy	L	32	1, 2, 3, 4, 5
Istituto di Radioastronomia	Noto, Italy	No	32	1, 2, 5
Hartebeesthoek Radio Astronomy Observatory	South Africa	E	26	4
Haystack Observatory	Westford, MA	K	37	1, 2, 3, 4, 5
National Radio Astronomy Observatory	Green Bank, WV	G	43	1, 2, 3, 4
George R. Agassiz Station	Fort Davis, TX	F	26	1, 2
National Radio Astronomy Observatory VLBA	Kitt Peak, AZ	Kp	25	2, 3, 4
National Radio Astronomy Observatory VLBA	Pie Town, NM	Pt	25	1, 2, 3, 4, 5
National Radio Astronomy Observatory VLBA	Los Alamos, NM	La	25	2, 3, 4, 5
National Radio Astronomy Observatory VLA	Socorro, NM	Y	25	2, 3, 5
National Radio Astronomy Observatory VLA	Socorro, NM	Y	25 (27 antennas)	4
Owens Valley Radio Observatory	Big Pine, CA	O	40	1, 2, 3, 4, 5

[a] Observing sessions defined in Table 2.

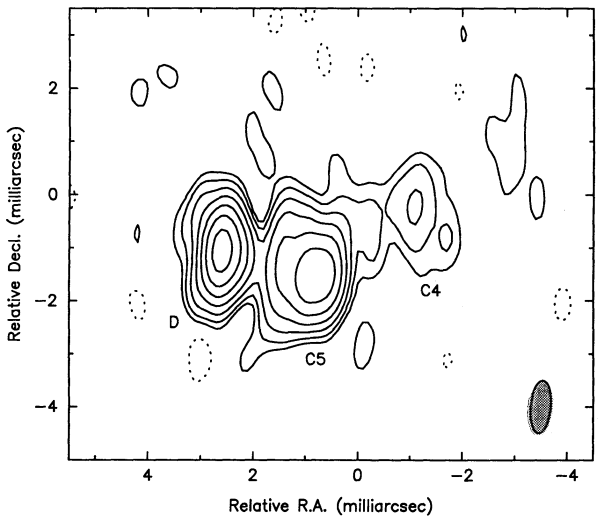

FIG. 3.—CLEAN image of 3C 345 at 10.7 GHz, epoch 1990.16 (Session 1 in Table 2). The CLEAN restoring beam (FWHM 1.00 × 0.40 mas in P.A. −5°) is shown as a shaded ellipse. Distinct features are labeled following the convention of BMC (§ 3.1). Coordinate origin is arbitrary. Contours are drawn at −10, 10, 20, 40, 80, 160, 320, and 640 mJy per beam; peak brightness is 959 mJy per beam. Except within 0.5 mas of "D" or "C5," the image should be reliable above the second contour level.

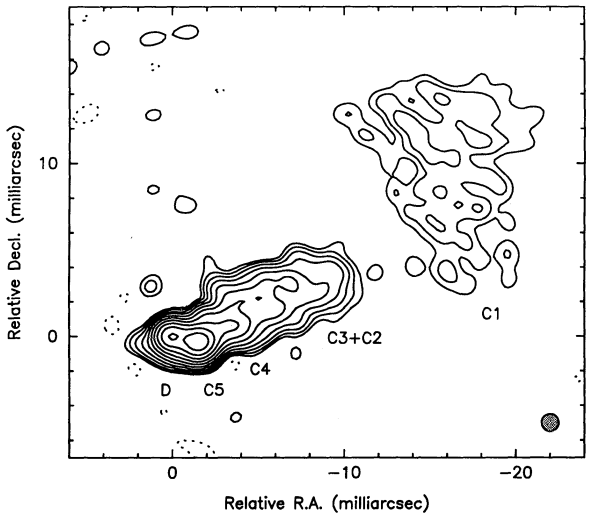

FIG. 4.—CLEAN image of 3C 345 at 5.0 GHz, epoch 1990.18 (Session 2). The CLEAN restoring beam (FWHM 1.00 mas) is shown as a shaded ellipse. Contours are drawn at −2, 2, 4, 8, 16, 32, 64, 128, 256, 512, and 1024 mJy per beam; peak brightness is 1726 mJy per beam. Except within 2 mas of "D" or "C5," the image should be reliable above the second contour level.

in the literature assume spherical components. The main drawback is that the agreement between the (u, v) data and the transform of the model is usually worse, because there are many fewer degrees of freedom. Although most of the following analysis is based on results from model fitting, we refer to the images when there were questions about the correspondence between model parameters and the features they represent.

3.3. *Component Spectra*

The results of model fitting the (u, v) data from the observations in Table 2 are shown in Figure 8 for components D, C5, and C4, together with the total source flux density. Plotted errors include two terms added in quadrature: (*a*) errors calculated using program ERRFIT (Pearson 1991) which yields 1 σ errors based on the agreement between data and model, which are probably underestimated because of strong correlations between variations in some parameters; and (*b*) uncertainties in the flux scale on the images (typically $\approx 10\%$). Only components D (the nucleus) and C5 are sufficiently well separated from adjacent features, or underlying jet emission, for model parameters to be completely reliable. At 1.7 GHz the resolution is too low to allow separation of D and C5; in Figure 8 we assumed the flux densities of 1.3 and 1.6 Jy, respectively, which is plausible because the spectrum of D is then relatively straight. Components seen on some of the images, but with poorly constrained spectra, are C6 and C3; the latter is confused with emission from the underlying jet, as noted by UW92 on the basis of high dynamic range 5 GHz images.

Except for the nucleus, all components for which fluxes can be measured show "normal" spectra (Kellermann & Pauliny-

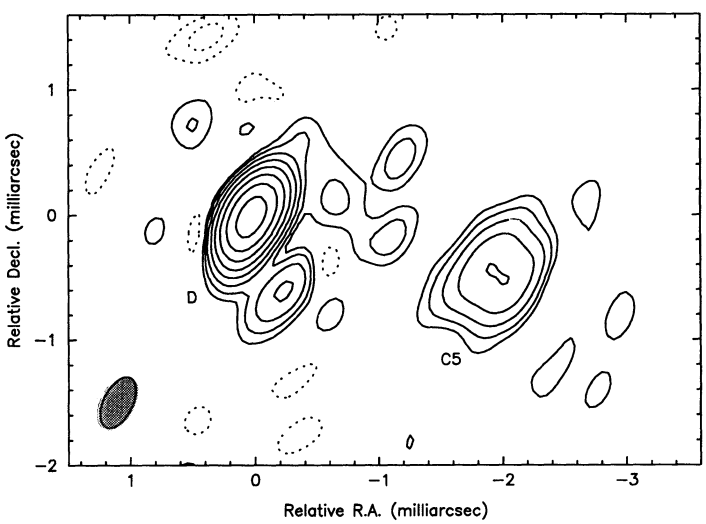

FIG. 5.—CLEAN image of 3C 345 at 22.2 GHz, epoch 1990.41 (Session 3). The CLEAN restoring beam (FWHM 0.44 × 0.24 mas in P.A. −27°) is shown as a shaded ellipse. Contours are drawn at −20, −10, 10, 20, 40, 80, 160, 320, 640, and 1280 mJy per beam; peak brightness is 1895 mJy per beam. The image is reliable above about the third contour level. Only "D" and "C5" are reliably detected; component "C6" (0.6 mas southwest of D) is a marginal detection due to considerable problems with amplitude calibration, as well as very poor weather at some sites.

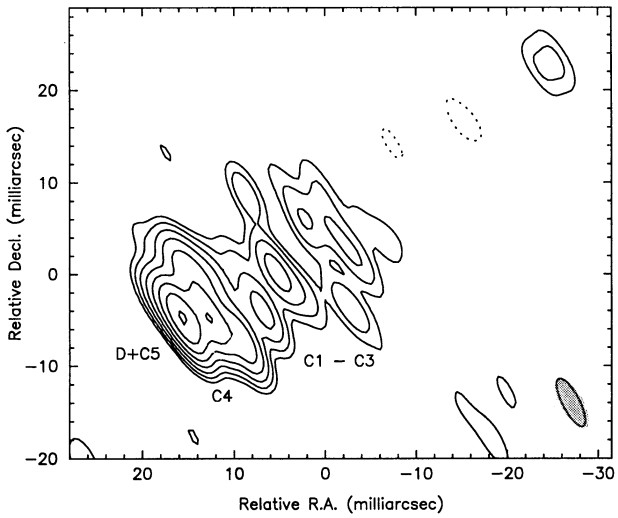

FIG. 6.—CLEAN image of 3C 345 at 1.7 GHz, epoch 1990.73 (Session 4). The CLEAN restoring beam (FWHM 5.8 × 1.9 mas in P.A. 29°) is shown as a shaded ellipse. Contours are drawn at −20, 20, 40, 80, 160, 320, 640, 1280, and 2560 mJy per beam; peak brightness is 2731 mJy per beam. This "snapshot" observation has a much lower dynamic range than the other images, but except within 4 mas of "D" or "C5," the image should be reliable above the third contour level.

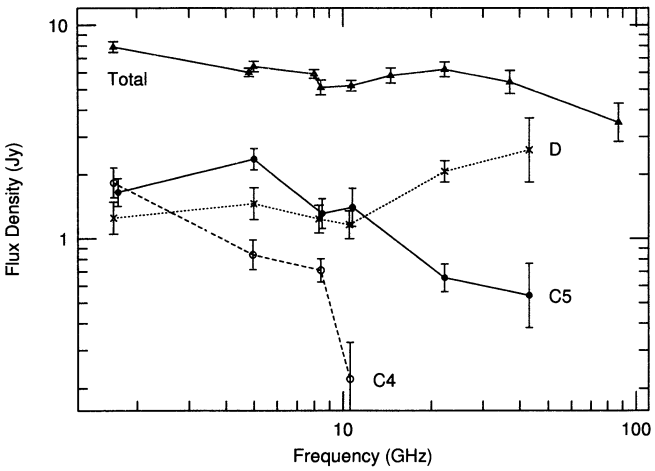

FIG. 8.—Radio spectrum of 3C 345 at epoch 1990.55. Straight lines are drawn between data points for clarity. Error bars represent ±1 σ errors from ERRFIT, plus an allowance of 10% for uncertainty in the flux scale (see text). Total flux data are from Table 2, an additional 5 GHz observation in 1991.70, H. Aller & M. Aller (private communication; 4.8, 8.0, and 14.5 GHz), and Teräsranta et al. 1992 (37 and 87 GHz). Also shown are the spectra of individual components as deduced from the images in Figs. 3–7 and model fitting of the (*u*, *v*) data. 43 GHz points are from J. A. Zensus (private communication). At 1.7 GHz components D and C5 are blended; we show the most plausible decomposition, in which the fluxes are roughly equal.

Toth 1969), with spectral indices in the range $\alpha = -0.5$ to -1.0. These components are consistent, in spectral shape at least, with simple synchrotron emission from a homogeneous sphere or slab. They are also in the same range as the measured X-ray spectral index (Table 1); this is expected for the SSC process of a homogeneous component because the X-ray spectrum derives from the scattering of radio-emitting "seed" photons.

The relative flatness of the total flux density curve in the 1–100 GHz range is due to the superposition of components with varying turnover frequencies. The nucleus itself has an almost flat spectrum, with $\alpha \approx +0.2$, in the range 1.7–43 GHz, characteristic of an inhomogeneous source. Interestingly, the fitted sphere diameter varies smoothly with frequency from 1.3 mas to 5 GHz to 0.2 mas at 22 GHz; these sizes are significantly above the resolution limit at each frequency. This trend is consistent with the Königl (1981) model, which we discuss further in the next section.

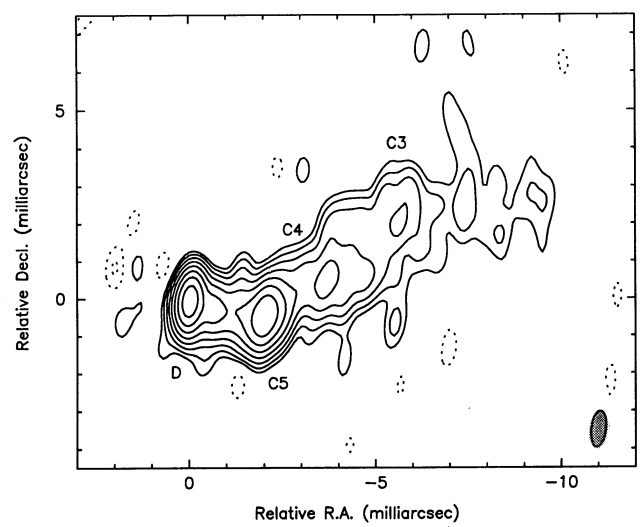

FIG. 7.—CLEAN image of 3C 345 at 8.4 GHz, epoch 1990.84 (Session 5). The CLEAN restoring beam (FWHM 0.97 × 0.42 mas in P.A. −7°) is shown as a shaded ellipse. Contours are drawn at −10, −5, 5, 10, 20, 40, 80, 160, 320, and 640 mJy per beam; peak brightness is 1058 mJy per beam. Except within 1 mas "D" or "C5," the image should be reliable above the second contour level.

4. MODELS OF X-RAY EMISSION

4.1. *Homogeneous Sphere Model*

Using the results from the previous section, we calculate the predicted inverse-Compton X-ray flux $S_{X,\mathrm{calc}}$ expected from each of the compact (parsec-scale) components in 3C 345. As explained in § 1, we use a simple homogeneous sphere model for components C4 and C5, and the Königl (1981) model for the nucleus. Departures from homogeneity do not invalidate the analysis but result in a modest underestimation of the X-ray flux (Hughes & Miller 1991); this leads to a lower limit to the Doppler factor δ derived from comparison with the observed X-ray flux $S_{X,\mathrm{obs}}$. If other processes contribute (including inverse-Compton emission from other compact components) then δ must be larger still, and estimates from the SSC calculation can be regarded as firm lower limits applying to each component separately.

Table 4 summarizes the observational data used to calculate $S_{X,\mathrm{calc}}$ (we used the formulae of Cohen 1985). For a homogeneous sphere, S_m, ν_m, and α define the spectrum completely. The measurements are most accurate for C5 because it is well separated from the other components (except at 1.7 GHz, where it is blended with D, as noted in § 3.3). The Doppler factor is not strongly dependent on the predicted flux; $\delta_{\mathrm{calc}} = (S_{X,\mathrm{calc}}/S_{X,\mathrm{obs}})^{1/(4-2\alpha)}$. Table 4 shows two possibilities for separating the model flux densities of C5 from D to 1.7 GHz and hence determining the spectral turnover. Taking the fluxes of D and C5 nearly equal, as shown in Figure 8, is the most plausible decomposition, and the "best-fit" parameters for C5 in Table 4 (row 2) are based on this decomposition; errors quoted represent the uncertainties in measuring S_m, ν_m, and α. Assuming that the nucleus (D) dominates over C5 yields a

TABLE 4

COMPONENT MODEL PARAMETERS

Component	S_m [a] (Jy)	ν_m (GHz)	α	ξ [b] (mas)	δ_{calc} [c]	D_{eq} [d]
C5[e]	3.0–5.0	2.0–5.0	−0.7 to −1.0	0.6–1.0	...	...
C5	3.2	2.7	−0.75	0.8	7.5	27
C5	2.3	5.0	−0.75	0.8	2.3	5
C4[f]	1.5–2.5	1.5–2.5	−0.6 to −0.9	2.4–3.0	...	...
C4	2.0	2.0	−0.75	2.7	1.0	2
D[g]	2.5	200	+0.2	0.18 at 22.2 GHz 0.32 at 10.7 GHz 0.60 at 8.4 GHz 1.31 at 5.0 GHz	4.6	...

[a] S_m = peak flux density (assuming a homogeneous sphere model), ν_m = "turnover" frequency.

[b] Angular diameter of homogeneous sphere, from model fitting. Range reflects variations between observing epochs, which dominate over the formal fitting errors.

[c] For components C4 and C5, the Doppler factor is calculated from the ratio of observed to model X-ray flux density. See § 4.2 for evaluation of δ for D.

[d] Equipartition Doppler factor D_{eq} (Readhead 1994).

[e] For C5, the first line gives the maximum range of each parameter consistent with the VLBI images and radio spectral data; certain parameter combinations are excluded by the data, so ranges of δ_{calc} or D_{eq} are not given. Second line represents the "best fit" parameter set; third line represents an alternative, but less consistent, fit (see § 4.1).

[f] For C4, the first line gives the maximum range of each parameter consistent with the VLBI images and radio spectral data; the second line represents the "best fit" parameter set, as discussed in § 4.1.

[g] Component D is the nucleus of 3C 345. Adopted parameters for the Königl 1981 inhomogeneous jet model; S_m, ν_m, and α correspond to what Königl calls $S_{obs,s}(\nu_{sM})$, ν_{sM}, and α_{s1} in that paper, respectively. Note that $\alpha_{s1} > 0$ results from the superposition of homogeneous components in the jet. The angular diameter is well fitted by a power law $\xi \propto \nu^{-1/k_m}$ with $k_m \approx 0.75$. Both α_{s1} and k_m are functions of the fundamental jet parameters α_0, m, and n (see § 4.2). Value not quoted for D_{eq} since it is a function of radius.

smaller Doppler factor, but this goes against the general observation that cores become less dominant at lower frequencies. We quote $\delta_{calc} = 7^{+3}_{-2}$, with the errors representing roughly a 68% confidence range for variations in all three parameters; we did not consider a full $\Delta\chi^2$ analysis necessary.

If we assume that C5 is the origin of *all* the X-ray emission then $\delta = \delta_{calc}$, which yields one relation between the fluid Lorentz factor $\gamma = (1 - \beta^2)^{-1/2}$, and θ, the angle of the jet axis to the line of sight. A second relation is the well-known formula for superluminal motion: $\beta_{obs} = \beta \sin\theta/(1 - \beta\cos\theta)$. Combining these, and taking the speed measured for C5 by UW92 ($\beta_{obs} = 7.0 \pm 1.0$), we find $\gamma = 7.5^{+1.0}_{-1.5}$ and $\theta = 8°^{+2°}_{-3°}$. We emphasize that within the above assumptions, *these values for γ and θ are probably the best determined of any AGN*. Virtually all other measurements to date have yielded only limits on, not measurements of, these kinematic quantities. They depend, of course, on the Hubble constant: for $h = 0.5$, we derive $\gamma = 18^{+8}_{-6}$ and $\theta = 6.°5 \pm 1.°5$.

For component C4, the computed value of δ_{calc} is consistent with no relativistic bulk motion (i.e., $\delta_{calc} \approx 1$). However, C4 is known from earlier studies to be superluminal (BMC) and must therefore be relativistic ($\gamma \gg 1$); except for the extreme case of $\gamma \gg 20$ (which we consider unlikely for other reasons; see § 5), this also implies $\delta > 1$, and hence $\delta > \delta_{calc}$. Thus we conclude that inverse-Compton emission from C4 does not contribute much to the observed X-ray flux at epoch 1990 July.

The values for C5 agree closely with earlier results referring to a different jet component, C3 (Unwin et al. 1983). At that epoch (1979.7), C3 was at a similar radius from the core as C5 is in our data. They measured $\beta_{obs} = 6.1$, $\delta > 8.1$, leading to firm limits $\theta < 7°$, $\gamma > 6$. That these limits are so close to our measured values for C5 is surely fortuitous, though it indicates that the jet geometry is not strongly time variable. Ghisellini et al. (1993) included 3C 345 as part of a large statistical study of superluminal motion and Doppler boosting. They quote $\delta = 5.3$, though the agreement with the present calculation is accidental, as they assume a much smaller angular size but higher turnover frequency—terms which tend to cancel out in deriving δ. Ghisellini et al. derive $\gamma \geq 37$, a large value which results from adopting a smaller Hubble constant ($h = 0.5$).

4.2. *Conical Jet Model*

In common with many compact radio sources, the nucleus of 3C 345 has a flat spectrum which is generally taken as an indication of inhomogeneity (Cotton et al. 1980; Marscher 1980). If we adopt the decomposition of D+C5 discussed above, then the core has a rising spectrum with $\alpha \approx +0.2$, and turnover frequency around 200 GHz. A flat spectrum arises naturally in the Königl (1981) model, which we now apply to the observational data on component D, using his formalism as implemented in a computer program by ZCU.

In this model, three parameters, α_0, m, and n, determine the spectral shape of the synchrotron and first-order inverse-Compton emission, integrated over the base of the jet, which we assume to be component D. The local electron energy spectrum is maintained with a power-law index $-2\alpha_0 + 1$, the magnetic field varies with radius down the jet as r^{-m}, and the particle density varies as r^{-n}. Although these parameters are not directly observable, we have measurements of three functions of them: α_{s1}, k_m, and α_{c2}, where $k_m = [(3 - 2\alpha_0)m + 2n - 2]/(5 - 2\alpha_0)$, $k_s = (1 - \alpha_0)m + n - 3$, $\alpha_{s1} = \alpha_0 + k_s/k_m$, and $\alpha_{c2} = \alpha_0 - (k_s + n - 1)/(7m - 4)$.

1. The (synchrotron) radio spectrum in this model is relatively flat, due to contributions from different radii (we measure $\alpha_{s1} = +0.2 \pm 0.2$; Fig. 8). This spectrum is maintained into the submillimeter, where we assume it dominates the total flux; the spectrum must steepen abruptly above the

turnover ($\alpha_{s2} \lesssim -1.0$). We estimate the turnover frequency and flux density by extrapolating the model spectrum to where it intersects the total flux spectrum (Königl's eqs. [3], [4], and [12]); hence $\nu_{sM} \approx 200$ GHz, $S_{\mathrm{obs},sM} \approx 2.5$ Jy.

2. The radius at which optically thin emission can be seen from the jet varies with frequency as a power law; the same relation applies to the angular size ξ of the nucleus if the jet opening angle is constant (i.e., $\xi \propto \nu^{-1/k_m}$). We have four measurements between 5.0 and 22.2 GHz of the diameters of spheres fitted to the data (§ 3.2); the emission region will not be spherical at any frequency, though the constant geometric factor does not enter the determination of k_m, which we measure with a (fortuitously) small formal error ($k_m = 0.75 \pm 0.02$).

3. The model inverse-Compton spectrum is curved, but in the X-ray range the index is Königl's parameter α_{c2} (≈ -0.9 from the *ROSAT* observation).

These relations do not yield unique solutions for α_0, m, and n. The best fit we obtained was $\alpha_0 = -0.6$, $m = 1.5$, and $n = 1.4$, corresponding to $\alpha_{s1} = +0.10$, $k_m = 1.15$, and $\alpha_{c2} = -0.79$, in fair agreement with observation. Hutter & Mufson (1986) derived similar values of m and n for three BL Lac objects (m ranging from 1.6 to 1.1, and n ranging from 1.1 to 1.6); they, however, assumed $\alpha_0 = -0.5$, and did not fit for k_m or α_{c2}.

Having estimated α_0, m, and n, we also need three quantities describing the jet dynamics: the opening angle of the jet (2ϕ), the fluid Lorentz factor (γ) and the angle of the jet axis to the line of sight (θ). None of these are directly observable, though we have contraints on functions of them. The *projected* cone angle $\phi_p = \phi/\sin\theta$ is measurable, at least for components well separated from the core. As an estimate of this quantity, we took the value of $\phi_p = 13°$ for the innermost jet component measured by BMC. The kinematic quantities γ and θ are constrained by the superluminal motion of C5. It is not clear whether values for C5 are applicable to the core: γ could be a function of radius, and since the jet "ridge" line is curved on the sky, θ could also vary (UW92). We initially adopted $\gamma = 7.5$ and $\theta = 8°$, but allowed them to vary, subject to the constraint $\beta_{\mathrm{obs}}(\gamma, \theta) = 7.0$ (see § 4.2 above). Since the X-ray flux is a strong function of θ, we evaluated $S_{X,\mathrm{calc}}(\gamma, \theta, \phi)$ (Königl's eq. [13]) over a wide range of θ, and then explored the effect of varying other parameters. Dependence on α_0, m, and n is relatively modest, so we left them at the values estimated from the above spectral constraints. Using the above set of jet parameters, the Königl model underpredicts the observed X-ray emission ($S_X > S_{X,\mathrm{calc}}$) by a factor of 5; we consider this fairly good agreement considering the uncertainties and assumptions involved (underprediction is an acceptable result; overprediction is not).

Our "best-fit" model to the available data yields agreement (i.e., $S_X = S_{X,\mathrm{calc}}$) if we increase θ to 11°.4, while holding other parameters (including ϕ_p) fixed. This does not, however, demonstrate that all the X-ray emission from 3C 345 must be inverse-Compton, only that it is consistent. Derived kinematic quantities are $\gamma = 7.7$, $\phi = 2°.6$, and $\delta = 4.6$. At 22 GHz, the jet emission dominates at a radius of 2.1 pc, corresponding to an angular distance of 0.11 mas from the apex of the cone; this is consistent with the core appearing almost unresolved in our 22 GHz (Fig. 5).

Important physical parameters derived from the best-fit model (using Königl's formalism again) are the magnetic field at a radius of 1 pc ($B_1 = 0.14$ G), the particle density at 1 pc ($K_1 = 2.5 \times 10^4$ cm^{-3}), and $r_M = 0.30$ pc (the radius within which optically thin radio emission contributes little to the overall spectrum). The jet is particle dominated at all radii $r \gtrsim 0.1$ pc; the ratio of particle energy density to magnetic energy density U_p/U_m increases rapidly with radius and is >100 at $r \geq 2$ pc. This is consistent with the radial dependences determined above: our value of $n = 1.4$ (i.e., <2) implies particle reacceleration in the jet, while $m = 1.5$ (i.e., $U_m \propto r^{-3.0}$) implies a radial dependence of magnetic field intermediate between purely radial and purely transverse field configurations.

The predicted X-ray flux is not strongly dependent on ϕ_p. If we reduce ϕ_p to 5°, then we get $S_X = S_{X,\mathrm{calc}}$ for $\theta = 9°.7$, corresponding to a very narrow cone ($\phi = 0°.8$). Likewise, if we assume that the spectrum of the core is in fact flat or falling with frequency, rather than rising (corresponding to $\alpha_{s1} \approx 0$, $\nu_{sM} \approx 300$ GHz and $S_{\mathrm{obs},sM} \approx 2.0$ Jy) we get $\theta = 11°.9$, $\gamma = 8.0$, $\phi = 2°.7$, and $\delta = 4.3$. VLBI imaging at 100 GHz or even higher is needed to determine whether the core spectrum continues rising into the millimeter wavelength range, as we have assumed here.

We conclude that the Königl jet model is capable of explaining the observed kinematic and spectral data for the nucleus of 3C 345, including the X-ray emission. In fact, the parameters of the "best-fit" jet model agree very well with the kinematic constraints derived for component C5 (§ 4.1). The agreement between the Doppler factors derived using two very different SSC models, $\delta \gtrsim 7$ and $\delta \gtrsim 4.6$, respectively, argues against large changes in jet geometry between the two scales involved (≈ 1.5 mas, or 40 pc deprojected for C5; $\lesssim 0.2$ mas, or $\lesssim 5$ pc deprojected for D).

4.3. *Equipartition Doppler Factors*

Readhead (1994) presents arguments that the brightness temperatures is powerful compact extragalactic radio sources are generally much less than the "inverse-Compton limit" of $T_b \sim 10^{12}$ K, and shows that the "equipartition brightness temperature" T_{eq}, derived from the equipartition angular size (Scott & Readhead 1977), is a more realistic limit. T_{eq} is very intensitive to measured parameters except δ, and it is typically $\approx 5 \times 10^{10}$ K. Readhead takes that as evidence that in most sources some mechanism must operate which prevents significant departures from equipartition. He defines the "equipartition Doppler factor" D_{eq} as a function of S_m, ν_m, and ξ (his S'_{op}, ν'_{op}, and θ), such that $\delta = D_{\mathrm{eq}}$ for a relativistic component in which equipartition holds between relativistic particle and magnetic field energy densities ($U_p/U_m = 1$). We now compute these quantities for components C4 and C5 in 3C 345, which we modeled as homogeneous spheres and for which this analysis readily applies.

First we calculated T'_{eq} for C4 and C5, using S_m and ν_m from Table 4 (all primed quantities are measured in our reference frame). This yields $T'_{\mathrm{eq}} = (6.1 \pm 0.1) \times 10^{10}\delta^{(13+2\alpha)/17}$ K and $(6.0 \pm 0.2) \times 10^{10}\delta^{(13+2\alpha)/17}$ K, respectively, where the errors represent the selection of extremes in the ranges given in Table 4. Then we computed the observed brightness temperature T'_b of the components of the peak frequency ν_m. Finally, we computed $D_{\mathrm{eq}}/\delta_{\mathrm{calc}} = T'_b/T'_{\mathrm{eq}}$, assuming for the purposes of this discussion that $\delta = \delta_{\mathrm{calc}}$ for each component (Table 4). It turns out that this ratio is not a strong function of the spectral turnover because the formulae for T'_b and δ_{calc} both involve S_m and ν_m raised to similar powers.

We conclude that components C4 and C5 in 3C 345 are strongly particle dominated, since $U_p/U_m = (D_{\mathrm{eq}}/\delta_{\mathrm{calc}})^{17/2} \sim 400$ for C4 and $\sim 5 \times 10^4$ for C5 (~ 600 for the less-plausible

high turnover frequency solution in Table 4). Independent estimates of δ_{calc} and D_{eq} are hard to derive without extensive VLBI data (such as we have here for 3C 345) because T'_{eq} depends on δ. Therefore, we do not regard this very first evaluation of D_{eq}/δ_{calc} to be in conflict with Readhead's conclusions. He points out that D_{eq} can be estimated for any source with a measured synchrotron self-absorption turnover. Our measurements suggest an application for this method: determining Doppler factors in a sample of sources statistically, if the ratio D_{eq}/δ does not vary strongly within the sample.

5. DISCUSSION AND SUMMARY

Contemporaneous X-ray and multiwavelength VLBI observations of 3C 345 have yielded excellent constraints on geometry, kinematics, and emission mechanism in this superluminal quasar, better than the constraints for any other AGN.

Several recent statistical studies of blazars and radio galaxies, addressing the issue of AGN unification, have argued that the radio and X-ray emission in blazars is beamed (Barthel 1989; Urry, Padovani, & Stickel 1991, and references therein; Padovani & Urry 1992). The present study presents a complementary approach, based on direct demonstration of relativistic beaming of the X-ray emission in a particular blazar. We applied self-consistent models of the expected inverse-Compton emission to detailed imaging of the parsec-scale radio emission in 3C 345. This source is one of a small number for which such a detailed analysis has been attempted. For 3C 345, at least, we conclude that the X-ray emission (at least from 0.2 to 10 keV) results from inverse-Compton emission in the parsec-scale radio jet.

More detailed study of the relation between radio and X-ray emission in blazars is currently limited to the incompleteness of most VLBI observations of AGNs, especially in the adequacy of temporal and wavelength coverage. The present work on 3C 345 represents the "state of the art" in VLBI monitoring, although even this is still insufficient to strongly constrain models for the jet emission. Clearly, the observational obstacles to extending even the present 3C 345 campaign to a reasonably sized sample of blazars are currently formidable. Multifrequency monitoring programs will become much easier with the advent of full VLBA operations; sources which vary much faster than 3C 345 (e.g., the radio galaxy 3C 120; Walker, Benson, & Unwin 1987) will become attractive targets for coordinated radio/X-ray campaigns.

Modeling single-epoch broad-band blazar spectra with an inhomogeneous jet model is a related but somewhat less well-constrained approach (e.g., Maraschi et al. 1992, and references therein). We saw in § 4.2 that even a relatively simple narrow-cone model has a large number of unconstrained model parameters, which renders derived quantities, such as the geometry or physical state of the jet, quite uncertain. Some parameters, such as Königl's (1981) power-law indices m and n, are apparently well-determined as other sources yield similar values to ours (e.g., the BL Lac objects studied by Hutter & Mufson 1986). They lead to the important conclusion that the relativistic jets in all these objects are magnetic field–dominated or in approximate equipartition with relativistic particles at small radii ($\ll 1$ pc), but become particle-dominated at larger radii. For components C4 and C5 we evaluated the equipartition Doppler factor and showed that $D_{eq} > \delta$ for a wide choice of parameters. This in turn implies that C4 and C5 are strongly particle dominated.

Our results for 3C 345 are all completely consistent with the beamed jet picture, with localized emission regions moving relativistically. In particular, we modeled the outwardly moving VLBI knots with a homogeneous SSC-emitting spheres, obtaining a useful lower limit to the Doppler factor, $\delta \gtrsim 7.5$, for the brightest knot, C5. This is completely consistent with the observed superluminal velocity of this component, $\beta_{obs} \approx 7$; combining the two values yields constraints on the Lorentz factor ($\gamma \gtrsim 7.5^{+1.0}_{-1.5}$) and the orientation ($\theta \lesssim 8^{\circ}{}^{+2^{\circ}}_{-3^{\circ}}$). If C5 is the origin of the X-rays, then these change from limits to firm values. If the Hubble constant is reduced then γ increases and θ decreases, as noted above.

The unresolved VLBI core of 3C 345 was modeled with an inhomogeneous conical jet (Königl 1981), which can explain both the shape of the radio spectrum of the nucleus and the observed X-ray flux density and spectral index. The resulting best estimate for the Doppler factor is $\delta \gtrsim 4.6$. Because there are more adjustable parameters than are well constrained by observation, the numerical predictions of this model are somewhat uncertain, but we can drawn the strong conclusion that $\delta \gg 1$ is required in order that the predicted X-ray flux not exceed that observed.

If the X-ray flux is in fact *not* dominated by the core, the predicted emission from a Königl jet must be reduced. This can be done most easily by reducing θ while holding the projected jet opening angle and other parameters constant. For instance, $S_X/S_{X,calc} \approx 5$ requires that θ be reduced to $\approx 7^{\circ}$, a value which is still consistent with other geometric constraints on the jet. The X-ray spectrum supports our interpretation of the X-ray emission as due to the inverse-Compton process; however, if the X-ray emission were in fact dominated by another process, such as bremsstrahlung from the inner part of a hot accretion disk (Saxton et al. 1993; although bremsstrahlung models fit our X-ray spectrum very poorly), then the estimated Lorentz factors of components C5 and D must be higher than the quoted limits. However, there may be theoretical grounds for excluding very large γ ($\gg 20$; Phinney 1987; Abramowicz 1992).

Recent VLBI imaging of 3C 345 (UW92, and this paper) has shown that the structure and evolution of the components is much more complicated than previously thought. There is no reason to believe that 3C 345 is unusual in any important respect (e.g., Pearson & Readhead 1988), so generalizations based on the properties of jets in large source samples must be approached with caution. However, the current work shows that higher angular resolution imaging at much higher radio (millimeter or submillimeter) frequencies would answer many of the above observational concerns. We can look forward to important advances when space-VLBI and millimeter-wavelength VLBI are able to make high dynamic range images.

We thank Marshall Cohen, who developed the original implementation of the X-ray formalism we use; and Alan Marscher, Alma Zook, and Greg Madejski for interesting discussions. We are grateful to Keith Thompson for assistance with VLBI imaging. Hugh Aller, Margo Aller, Harri Terästranta, and Esko Valtaoja kindly provided flux-density monitoring data in advance of publication. The radio data presented here were provided by participating observatories of the US and European VLBI Networks; we thank them for their cooperation. Telescopes at Haystack, NRAO Green Bank, NRAO VLA and VLBA, Fort Davis and OVRO are supported by the National Science Foundation. This work was supported in part by NSF grant AST-9117100 to the Owens Valley Radio Observatory, and NASA grants NAG5-1582 and NAG5-1918 from the *ROSAT* Guest Observer Program.

REFERENCES

Abramowicz, M. A. 1992, in Extragalactic Radio Sources—From Beams to Jets, ed. J. Roland, H. Sol, & G. Pelletier (Cambridge: Cambridge Univ. Press), 206
Barthel, P. D. 1989, ApJ, 336, 606
Band, D. L., & Grindlay, J. E. 1985, ApJ, 298, 128
———. 1986, ApJ, 308, 576
Biretta, J. A., Moore, R. L., & Cohen, M. H. 1986, ApJ, 308, 93 (BMC)
Blandford, R. D., & Königl, A. 1979, ApJ, 232, 34
Blandford, R. D., & Rees, M. J. 1992, in Testing in the AGN Paradigm, ed. S. S. Holt, S. J. Neff, & C. M. Urry (New York: AIP), 3
Celotti, A., Maraschi, L., & Treves, A. 1991, ApJ, 377, 403
Cohen, M. H. 1985, in Extragalactic Energetic Sources, ed. V. K. Kapahi (Bangalore: Indian Academy of Sciences), 1
Cotton, W. D., et al. 1980, ApJ, 238, L123
Elvis, M., Lockman, F. J., & Wilkes, B. J. 1989, AJ, 97, 777
George, I. M., Warwick, R. S., & Bromage, G. E. 1988, MNRAS, 232, 793
Ghisellini, G., Maraschi, L., & Treves, A. 1985, A&A, 146, 204
Ghisellini, G., Padovani, P., Celotti, A., & Maraschi, L. 1993, ApJ, 407, 65
Giommi, P., Barr, P., Garilli, B., Maccagni, D., & Pollock, A. M. T. 1990, ApJ, 356, 432
Halpern, J. P. 1982, PhD thesis, Harvard Univ.
Hasinger, G., Turner, T. J., George, I. M., & Boese, G. 1992, Legacy, 2, 77
Hughes, P. A., & Miller, L. 1991, in Beams and Jets in Astrophysics, ed. P. A. Hughes (Cambridge: Cambridge Univ. Press), 1
Hutter, D. L., & Mufson, S. L. 1986, ApJ, 301, 50
Impey, C. D., & Neugebauer, G. 1988, AJ, 95, 307
Jones, T. W., O'Dell, S. L., & Stein, W. A. 1974, ApJ, 188, 353
Kellermann, K. I., & Pauliny-Toth, I. I. K. 1969, ApJ, 155, L71
Königl, A. 1981, ApJ, 243, 700
Kollgaard, R. I., Wardle, J. F. C., & Roberts, D. H. 1989, AJ, 97, 1550
Ku, W. H.-M., Helfand, D. J., & Lucy, L. B. 1980, Nature, 288, 323
Makino, F. 1989, in AGN and the X-Ray Background (Proc. 23rd ESLAB Symp.), ed. J. Hunt & B. Battrich (Noordwijk: ESA), 2, 803
Maraschi, L., Ghisellini, G., & Celotti, A. 1992, in Testing the AGN Paradigm, ed. S. S. Holt, S. J. Neff, & C. M. Urry (New York: AIP), 439
Marscher, A. P. 1980, ApJ, 235, 386
Marscher, A. P., & Broderick, J. J. 1985, ApJ, 290, 735
Marscher, A. P., & Gear, W. K. 1985, ApJ, 298, 114
Moffet, A. T., Gubbay, J., Robertson, D. S., & Legg, A. J. 1972, in IAU Symp. 44, External Galaxies and Quasi-Stellar Objects, ed. D. S. Evans (Dordrecht: Reidel), 228
Moore, R. L., & Stockman, H. S. 1984, ApJ, 279, 465
Murphy, D. W., Browne, I. W. A., & Perley, R. A. 1993, MNRAS, 264, 298
Padovani, P., & Urry, C. M. 1992, ApJ, 387, 449
Pearson, T. J. 1990, in Parsec-Scale Radio Jets, ed. J. A. Zensus & T. J. Pearson (Cambridge: Cambridge Univ. Press), 1
———. 1991, BAAS, 23, 991
Pearson, T. J., & Readhead, A. C. S. 1988, ApJ, 328, 114
Pfeffermann, E., et al. 1986, Proc. SPIE, 733, 519
Phinney, E. S. 1987, in Superluminal Radio Sources, ed. J. A. Zensus & T. J. Pearson (Cambridge: Cambridge Univ. Press), 301
Readhead, A. C. S. 1994, ApJ, 426, 51
Reid, M. J., Biretta, J. A., Junor, W., Muxlow, T. W. B., & Spencer, R. E. 1989, ApJ, 336, 112
Saxton, R. D., Turner, M. J. L., Williams, O. R., Stewart, G. C., Ohashi, T., & Kii, T. 1993, MNRAS, 262, 63
Scott, M. A., & Readhead, A. C. S. 1977, MNRAS, 180, 539
Sembay, S., Warwick, R. S., Urry, C. M., Sokoloski, J., George, I. M., Makino, F., Ohashi, T., & Tashiro, M. 1993, ApJ, 404, 112
Shafer, R. A., Haberl, F., Arnaud, K. A., & Tennant, A. F. 1990, XSPEC Users' Guide, Version 2 (Noordwijk: ESA TM-09)
Teräsranta, H., et al. 1992, A&AS, 94, 121
Unwin, S. C., Cohen, M. H., Pearson, T. J., Seielstad, G. A., Simon, R. S., Linfield, R. P., & Walker, R. C. 1983, ApJ, 271, 536
Unwin, S. C., & Wehrle, A. E. 1992, ApJ, 398, 74 (UW92)
Urry, C. M., Padovani, P., & Stickel, M. 1991, ApJ, 382, 501
Walker, R. C., Benson, J. M., & Unwin, S. C. 1991, in Superluminal Radio Sources, ed. J. A. Zensus T. J. Pearson (Cambridge: Cambridge Univ. Press), 48
Webb, J. R., et al. 1994, ApJ, 422, 570
Wehrle, A. E., et al. 1994, in preparation
Worrall, D. M., & Wilkes, B. J. 1990, ApJ, 360, 396
Worrall, D. M., et al. 1992, in Data Analysis in Astronomy IV, ed. V. Di Gesu et al. (New York: Plenum), 145
Zensus, J. A., Cohen, M. H., & Unwin, S. C. 1994, ApJ, submitted (ZCU)